Article

Rational Photodeposition of Cobalt Phosphate on Flower-like ZnIn$_2$S$_4$ for Efficient Photocatalytic Hydrogen Evolution

Yonghui Wu [1], Zhipeng Wang [1], Yuqing Yan [1], Yu Wei [1], Jun Wang [1], Yunsheng Shen [1], Kai Yang [1], Bo Weng [2] and Kangqiang Lu [1,*]

[1] Jiangxi Provincial Key Laboratory of Functional Molecular Materials Chemistry, School of Chemistry and Chemical Engineering, Jiangxi University of Science and Technology, Ganzhou 341000, China
[2] cMACS, Department of Microbial and Molecular Systems, KU Leuven, 3001 Leuven, Belgium
* Correspondence: kqlu@jxust.edu.cn

Abstract: The high electrons and holes recombination rate of ZnIn$_2$S$_4$ significantly limits its photocatalytic performance. Herein, a simple in situ photodeposition strategy is adopted to introduce the cocatalyst cobalt phosphate (Co-Pi) on ZnIn$_2$S$_4$, aiming at facilitating the separation of electron–hole by promoting the transfer of photogenerated holes of ZnIn$_2$S$_4$. The study reveals that the composite catalyst has superior photocatalytic performance than blank ZnIn$_2$S$_4$. In particular, ZnIn$_2$S$_4$ loaded with 5% Co-Pi (ZnIn$_2$S$_4$/5%Co-Pi) has the best photocatalytic activity, and the H$_2$ production rate reaches 3593 μmol·g^{-1}·h^{-1}, approximately double that of ZnIn$_2$S$_4$ alone. Subsequent characterization data demonstrate that the introduction of the cocatalyst Co-Pi facilitates the transfer of ZnIn$_2$S$_4$ holes, thus improving the efficiency of photogenerated carrier separation. This investigation focuses on the rational utilization of high-content and rich cocatalysts on earth to design low-cost and efficient composite catalysts to achieve sustainable photocatalytic hydrogen evolution.

Keywords: photocatalytic H$_2$ evolution; indium zinc sulfide; cocatalyst; cobalt phosphate; photogenerated holes transfer

1. Introduction

Rapid economic and social development depends on fossil fuels. However, due to the non-renewable nature of fossil fuels and the detrimental impact on the environment, it is imperative that we urgently seek sustainable energy sources capable of replacing them [1–5]. Hydrogen (H$_2$) energy, as a clean and renewable energy source, is one of the most promising alternative energy sources for fossil fuels [6–8]. Among various H$_2$ production methods, solar-driven water splitting for H$_2$ production is considered as a green and sustainable solar energy conversion technology, which can relieve the pressure of energy dilemma and environmental pollution [9–12]. Consequently, there is an urgent need to develop photocatalysts with high performance to promote the application of photocatalytic H$_2$ evolution technology [13]. Nowadays, due to their remarkable light absorption properties and special electronic structures, metal sulfides have become a hot topic in the field of solar energy conversion technology.

As a ternary sulfide, ZnIn$_2$S$_4$ has attracted global attention from researchers on account of its favorable layered structure, simple synthesis, good photostability and suitable electronic band structure [14,15]. In particular, the flower-like structure has a high surface area and improves the light absorption through multiple reflections, which plays an important role in enhancing the photocatalytic performance [16–18]. However, due to the high recombination rate of photogenerated electron–hole pairs, pure ZnIn$_2$S$_4$ exhibits low photocatalytic activity [19–22]. To address this problem, the rational introduction of cocatalyst is a viable approach to optimize the activity and stability of ZnIn$_2$S$_4$ [23]. Among the many cocatalysts, cobalt phosphate (Co-Pi) has demonstrated remarkable ability to transfer photogenerated holes from different light-collecting semiconductors in previous

studies and has been reported to improve their overall performance [24]. Therefore, the rational introduction of the holes cocatalyst Co-Pi into $ZnIn_2S_4$ is expected to obtain a cost-effective and efficient composite photocatalyst to promote photocatalytic H_2 evolution. Moreover, in situ photodeposition is considered to be a promising method to enhance the photocatalytic activity of semiconductors, due to its advantages such as close contact, simple preparation and directional loading [25–27]. Consequently, rationally introducing Co-Pi into $ZnIn_2S_4$ by in situ photodeposition is expected to promote the migration of photogenerated holes of $ZnIn_2S_4$, thereby improving the photocatalytic performance of the composite photocatalyst.

Herein, we prepare the $ZnIn_2S_4$ nanoflower substrate material by the hydrothermal method, and the hybrid catalyst is constructed by in situ photodeposition of cobalt phosphate (Co-Pi) on $ZnIn_2S_4$ nanoflower. The $ZnIn_2S_4$/Co-Pi composite exhibits a significantly enhanced performance in the photocatalytic H_2 evolution compared to pure $ZnIn_2S_4$. Notably, the optimal $ZnIn_2S_4$/5%Co-Pi photocatalytic H_2 production rate is 3593 $\mu mol \cdot g^{-1} \cdot h^{-1}$, which surpasses most similar hybrid cocatalyst systems reported in the literature (Table 1). The photo/electrochemical tests and photoluminescence (PL) confirm that the photogenerated carrier separation efficiency of the composite catalyst is significantly improved. This work aims to provide insights for designing cost-effective and efficient mixed catalysts to enhance overall photocatalytic performance through rationally exploiting earth-abundant cocatalysts.

Table 1. Comparison of the hydrogen production properties of the $ZnIn_2S_4$-based catalysts.

Photocatalysts	Light Sources	Sacrificial Agents	H_2 ($\mu mol \cdot g^{-1} \cdot h^{-1}$)	Reference
$ZnIn_2S_4$-5%Co-Pi	300 W Xe lamp ($\lambda \geq 420$ nm)	TEOA	3593	this work
$ZnIn_2S_4$/$NiWO_4$	300 W Xe lamp ($\lambda \geq 420$ nm)	TEOA	1781	[28]
$ZnIn_2S_4$/BPQDs	300 W Xe lamp ($\lambda \geq 420$ nm)	TEOA	1207	[29]
J-$ZnIn_2S_4$/$CdIn_2S_4$	350 W Xe lamp ($\lambda \geq 420$ nm)	TEOA	1830	[30]
N-$ZnIn_2S_4$	350 W Xe lamp ($\lambda \geq 400$ nm)	Na_2S/Na_2SO_3	262.62	[31]
MoO_2/$ZnIn_2S_4$	300 W Xe lamp ($\lambda \geq 420$ nm)	TEOA	2722.5	[32]
ReS_2/$ZnIn_2S_4$	four 3 W 420 nm LED lamps	lactic acid (10 vol%)	2240	[33]
$ZnIn_2S_4$/$CoFe_2O_4$	300 W Xe lamp ($\lambda \geq 420$ nm)	Na_2S/Na_2SO_3	2260.5	[16]
$NiCo_2S_4$/$ZnIn_2S_4$	Xe lamp ($\lambda > 400$ nm)	-	770	[34]
$CoS_{1.097}$/$ZnIn_2S_4$	300 W Xe lamp (780 nm $\geq \lambda \geq 420$ nm)	TEOA	2632.33	[35]

2. Results and Discussion

The preparation process diagram of the $ZnIn_2S_4$/Co-Pi (ZIS/Co-Pi) composite is shown in Figure 1a. Initially, $ZnIn_2S_4$ (ZIS) nanoflower is prepared by a one-step hydrothermal process. Subsequently, Co-Pi is introduced to ZIS nanoflower by in situ photodeposition to obtain ZIS/Co-Pi composites. Due to the best photocatalytic H_2 production performance of $ZnIn_2S_4$/5%Co-Pi (Z5CP), we mainly discuss this proportion of the composites in the subsequent characterization. According to Figure S1a,b, the color of ZIS nanoflower changes significantly before and after in situ photodeposition, with pure ZIS appearing as bright yellow, and Z5CP appearing as yellowish green. The morphology and microstructure of different samples are obtained by field emission scanning electron microscopy (FESEM). As depicted in Figure 1b, pure ZIS presents a spherical flower-like structure with a diameter of about 1 μm. The SEM image of Z5CP (Figure 1c) shows

that Z5CP inherits the flower-like structure of ZIS. Notably, the flower-like structure can provide a number of active sites, and multiple layers of petals enable light to be reflected multiple times, which leads to enhanced light absorption [36,37]. In addition, the SEM image of Z5CP shows that the Co-Pi nanoparticles are highly dispersed, and no large Co-Pi particles were observed. As presented in Figure 1d, transmission electron microscopy (TEM) characterization further confirms the spherical flower-like structure of ZIS. Moreover, Figure 1e shows that the Co-Pi nanoparticles are attached to the ZIS nanoflower, proving the successful synthesis of Z5CP composites. As depicted in Figure 1f, the lattice distance of Z5CP is about 0.297 nm corresponding to the (104) crystal face of ZIS, and the Co-Pi synthesized by in situ photodeposition is amorphous. Furthermore, the EDS spectra (Figure S2) and the element mapping results (Figure 1g) confirm the existence of Zn, In, S, P, O, and Co elements in Z5CP. The spatial distribution of Zn, In, S, O, P, and Co elements in the elemental mapping images of Z5CP composite shows that Co-Pi grows uniformly on the surface of ZIS nanoflower.
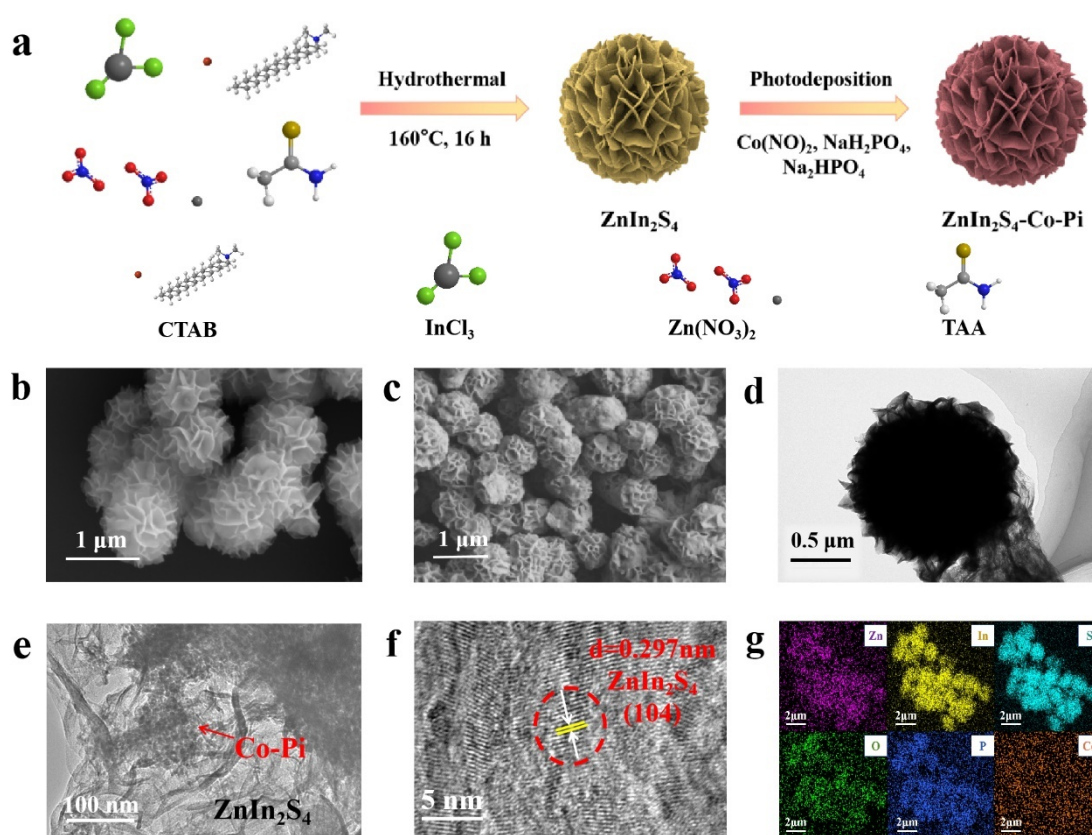
Figure 1. (**a**) Diagram illustrating the synthesis of ZIS/Co-Pi. (**b**,**c**) FESEM images of ZIS and Z5CP. (**d**–**f**) TEM images of Z5CP. (**g**) Mapping analysis results of Z5CP.

The phase structure and crystallinity are analyzed by the X-ray diffraction (XRD) map. Figure 2a displays the XRD spectra of both ZIS and Z5CP. For ZIS, the strong diffraction peaks at 27.5° and 47.2° belong to the (102) and (110) faces of hexagonal ZIS (JCPDS No.65-2023) [38]. For Z5CP composites, the XRD diffraction curve closely resembles that of ZIS except that there is a faint peak at 55.6° belonging to the (202) face of hexagonal ZIS, indicating that ZIS remains a stable crystal structure after coupling with Co-Pi [39]. However, in the Z5CP composite, the characteristic diffraction peak of Co-Pi is not observed due to the amorphous nature of in situ photodeposition of Co-Pi [40,41]. The optical characteristics of the photocatalysts are analyzed by UV-visible diffuse reflection spectroscopy (DRS). As depicted in Figure 2b, the pure ZIS displays a clear absorption edge around 520 nm, indicating a band gap of about 2.44 eV [42]. Compared with pure ZIS, the absorption intensity

of Z5CP hybrid in the visible range (520~750 nm) increases with the strong absorption of Co-Pi, indicating that the introduction of Co-Pi can improve the visible light response of ZIS. Moreover, Figure 2b shows that there is no significant shift in absorption edge for the Z5CP composite, indicating that the Co-Pi cocatalyst only deposits on the ZIS surface and does not bind with the crystal lattice.
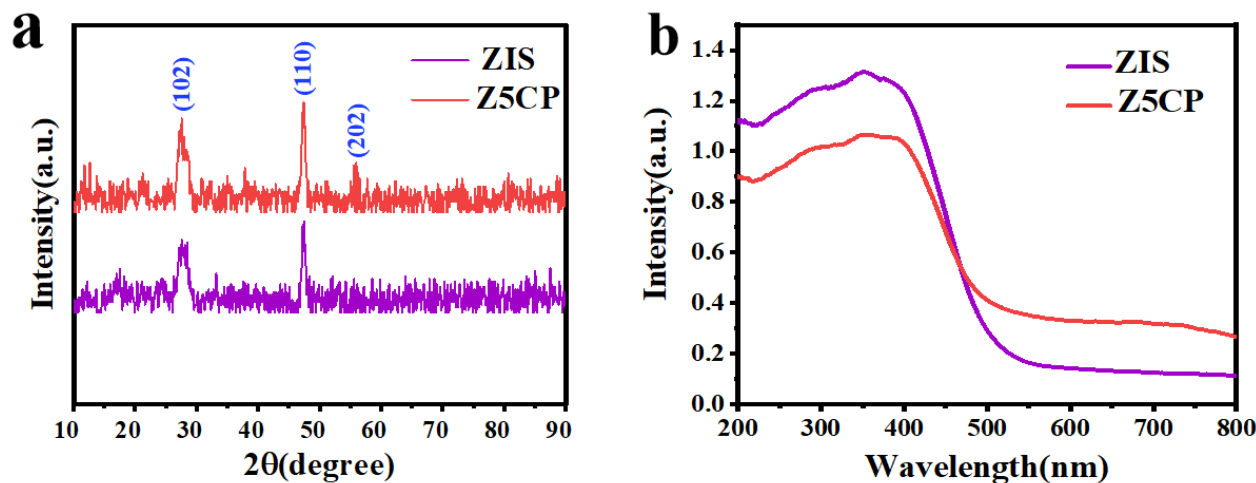
Figure 2. (**a**) X-ray diffraction (XRD) patterns and (**b**) UV–vis diffuse reflectance spectra (DRS) of ZIS and Z5CP.

The chemical composition and elemental states of Z5CP composite are further determined by X-ray photoelectron spectroscopy (XPS). As presented in Figure 3a, Zn, In, S, Co, and P elements exist in the hybrid products, which further demonstrates the successful photodeposition of Co-Pi on the surface of ZIS nanoflower. As shown in Figure 3b, the XPS spectrum of Zn 2p exhibits two distinct peaks at 1045 and 1022 eV, which correspond to the binding energies of Zn $2p_{1/2}$ and Zn $2p_{3/2}$ of Zn^{2+}, respectively. From the XPS spectrum of In 3d (Figure 3c), two peaks that center on binding energies 452.4 and 444.8 eV are respectively associated with In $3d_{3/2}$ and In $3d_{5/2}$, which indicate the +3 state of In. Moreover, as presented in Figure 3d, the peaks of 162.9 and 161.7 eV belong to S $2p_{1/2}$ and S $2p_{3/2}$, confirming the presence of S^{2-}. In the XPS spectrum of Co 2p (Figure 3e), the peak of Co $2p_{3/2}$ is at 781.3 eV (satellite peak at 784.3 eV), indicating the presence of Co^{2+} in the Z5CP composite [43–45]. In addition, the peak of P 2p (Figure 3f) at 133.5 eV indicates that P presents in the form of phosphate groups, which further proves the successful synthesis of Z5CP [46].

Photocatalytic H_2 production is performed with triethanolamine (TEOA) as the hole scavenger, and the photocatalytic properties of pure ZIS and different proportions of ZIS/Co-Pi composites under visible light are investigated. Figure 4a is a diagram of the photocatalytic activity of ZIS and composite with 1%, 5%, and 10% Co-Pi (hereinafter shown as Z1CP, Z5CP, and Z10CP, respectively). As shown in Figure 4a, due to the fast photogenerated electron–hole recombination rate, the pure ZIS is less active and the H_2 evolution rate is only 1832 $\mu mol \cdot g^{-1} \cdot h^{-1}$. After the introduction of Co-Pi cocatalyst, Z1CP, Z5CP, and Z10CP all show better H_2 evolution performance compared with blank ZIS. With the increase in Co-Pi content, the hydrogen yield increases gradually. However, when the Co-Pi content increases further, the H_2 evolution activity decreases, which may be due to the remarkable shielding effect of Co-Pi, thereby decreasing the photocatalytic active sites [47]. In particular, the Z5CP composite shows the highest H_2 evolution rate (3593 $\mu mol \cdot g^{-1} \cdot h^{-1}$), approximately two times higher than that of ZIS alone. This can be attributed to the fact that in situ photodeposition of Co-Pi promotes the transfer of photogenerated holes and reduces the recombination rate of photogenerated carriers. As shown in Table 1, the Z5CP composite prepared in this work has optimal photocatalytic H_2 production properties compared with the photocatalytic H_2 production activities of some

representative ZIS-based composites reported in recent years. In addition, the stability of Z5CP is tested by the cyclic test. As depicted in Figure 4b, after five cycles, no apparent deactivation has been observed for Z5CP composite, indicating the excellent stability of Z5CP composite.
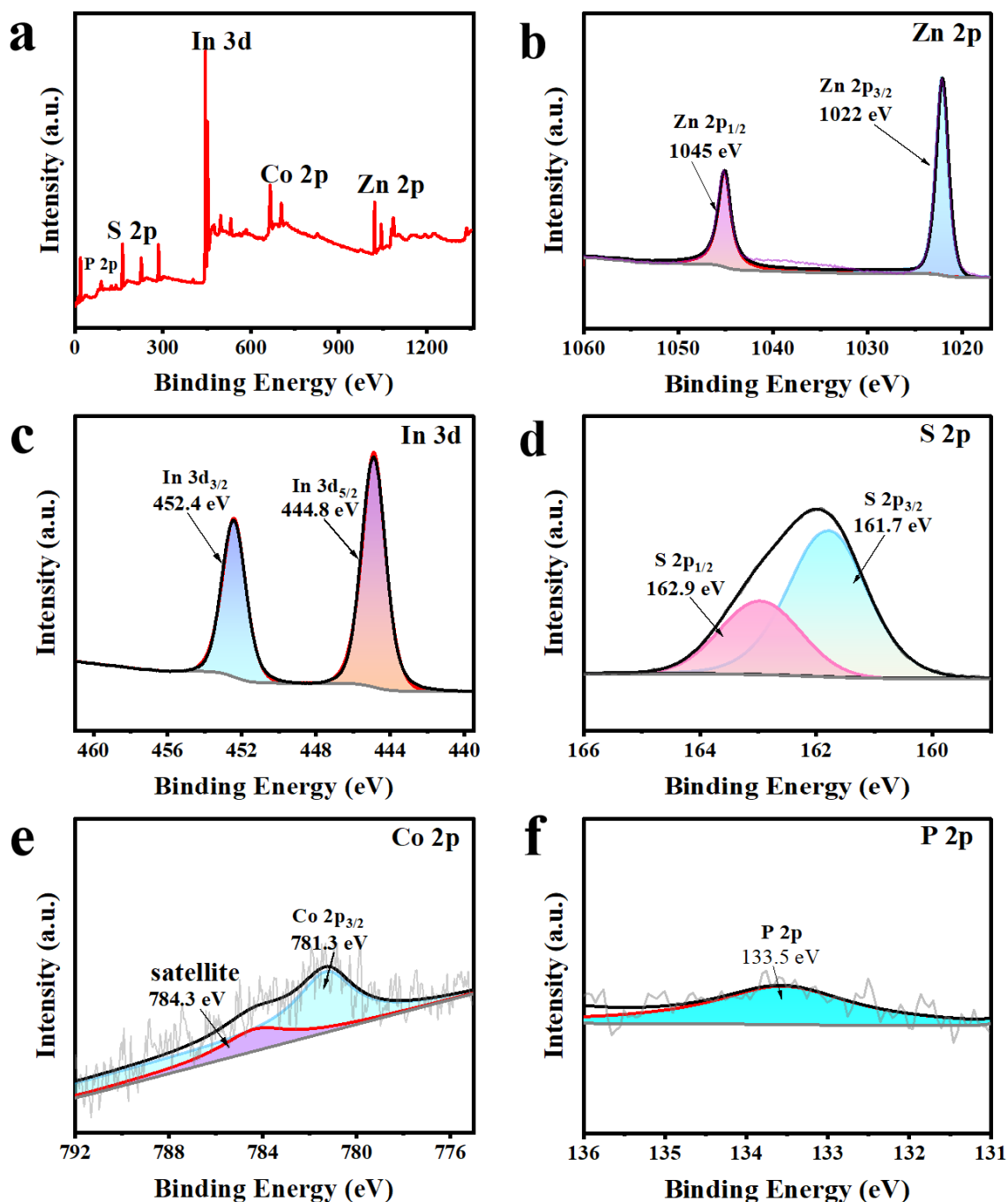
Figure 3. (**a**) XPS spectra of Z5CP, high-resolution spectra of (**b**) Zn 2p, (**c**) In 3d, (**d**) S 2p, (**e**) Co 2p, (**f**) P 2p.
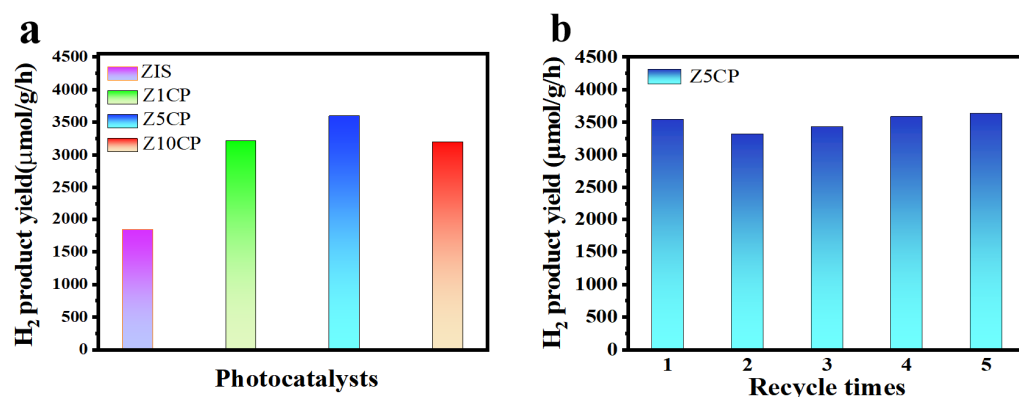
Figure 4. (**a**) Photocatalytic H_2 production over pure ZIS and Z5CP composites. (**b**) Stability plots of the photocatalytic H_2 production by Z5CP.

Photo/electrochemical tests are used to further characterize material reducing capacity and photogenerated carrier transfer efficiency. Linear sweep voltammetry (LSV) is first used to determine the H_2 evolution performance of ZIS and Z5CP samples. Figure 5a shows the polarization curve of ZIS and Z5CP composites. It can be seen that the overpotential of Z5CP is less than ZIS at the same current density, indicating that the H_2 evolution performance of Z5CP is better than that of ZIS [48]. The kinetics of photocatalysis in different samples can be compared by the Tafel slope. As shown in Figure S3, the Tafel slope of the Z5CP composite (0.21 V/decade) is smaller than that of ZIS (0.24 V/decade), indicating the better reduction effect and interfacial charge transfer efficiency of Z5CP, which is consistent with the photocatalytic H_2 production activity as well as other characterization results [49]. These results further demonstrate that Z5CP has faster reaction kinetics and excellent interface carrier separation efficiency. To study the charge separation and transfer of these ZIS/Co-Pi composites, instantaneous photocurrent (IT), electrochemical impedance spectroscopy (EIS) and steady-state photoluminescence (PL) spectra are measured on the ZIS and Z5CP samples [50]. As illustrated in Figure 5b, the optical current density of ZIS is small, indicating that the photogenerated carrier separation efficiency of ZIS is poor. However, it is found that after the introduction of Co-Pi, the optical current density of Z5CP is significantly improved compared with that of pure ZIS, indicating that Z5CP has better separation efficiency of electron (e^-) and hole (h^+) [51–55]. As shown in Figure 5c, the radius of curvature of Z5CP composite is smaller than ZIS, indicating that the charge transfer resistance of Z5CP is lower, which improves the separation and transfer rate of photogenerated carriers, thus enhancing the photocatalytic activity [56–60]. Furthermore, Figure 5d describes the steady−state photoluminescence (PL) spectra test of the sample. As shown in Figure 5d, the PL intensity of Z5CP is significantly lower than that of blank ZIS, indicating that the addition of cocatalyst Co-Pi effectively inhibits the recombination of photogenerated carriers [61–65]. Taken together, the results of these photo/electrochemical tests validate the improved separation and transfer of photogenerated charges in Z5CP, leading to the enhanced performance of photocatalytic H_2 evolution.

The information of chemical reaction area of the blank ZIS and the composite material Z5CP is obtained by the cyclic voltammetry test (CV). Figure 6a,b show the cyclic voltammetry (CV) curves of the blank ZIS and Z5CP composites, respectively. As illustrated in Figure 6c, the double-layer capacitance of Z5CP composite (3.99 $\mu F \cdot cm^{-2}$) is significantly larger than ZIS (1.83 $\mu F \cdot cm^{-2}$), which strongly proves that Z5CP has more active sites area than ZIS [45]. In addition, the flat charged position (E_{fb}) of the original ZIS is measured with Mott–Schottky (MS). Generally, the slope of the positive one indicates that the semiconductor is an intrinsic n-type semiconductor [51]. As can be seen from Figure 6d, ZIS belongs to the n-type semiconductor. Moreover, Figure S4 shows the detailed fitting parameters of MS. According to the x-intercept of the block, its E_{fb} is determined to be −0.52 V (vs. Ag/AgCl). In general, the conduction band position of n-type semiconductors

is about 0.2 V more negative than that of E_{fb} [66–68]. Therefore, the conduction charge position (E_{CB}) of the ZIS is -0.72 V (vs. Ag/AgCl). From the formula $E_{NHE} = E_{Ag/AgCl} + 0.20$ V, the E_{CB} of ZIS is -0.52 V (vs. NHE). According to the band gap of ZIS (2.44 eV), the valence band potential (E_{VB}) of ZIS is 1.92 V (vs. NHE).
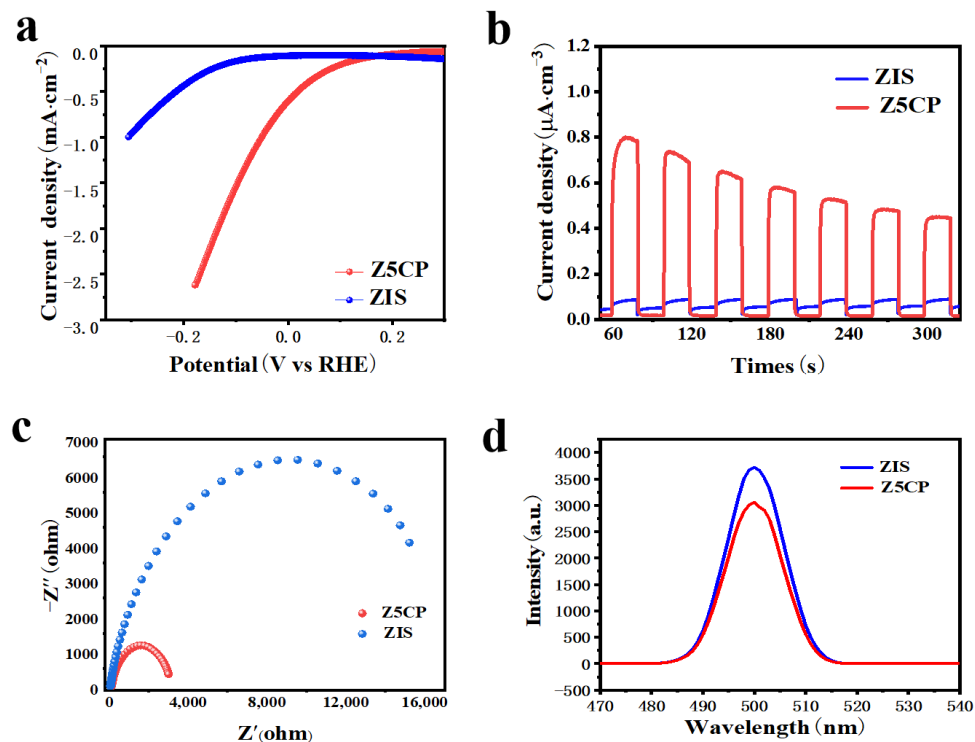
Figure 5. (**a**) Polarization curves. (**b**) Transient photocurrent spectra. (**c**) EIS Nyquist plots. (**d**) Steady−state photoluminescence (PL) emission spectra with an excitation wavelength of 500 nm.
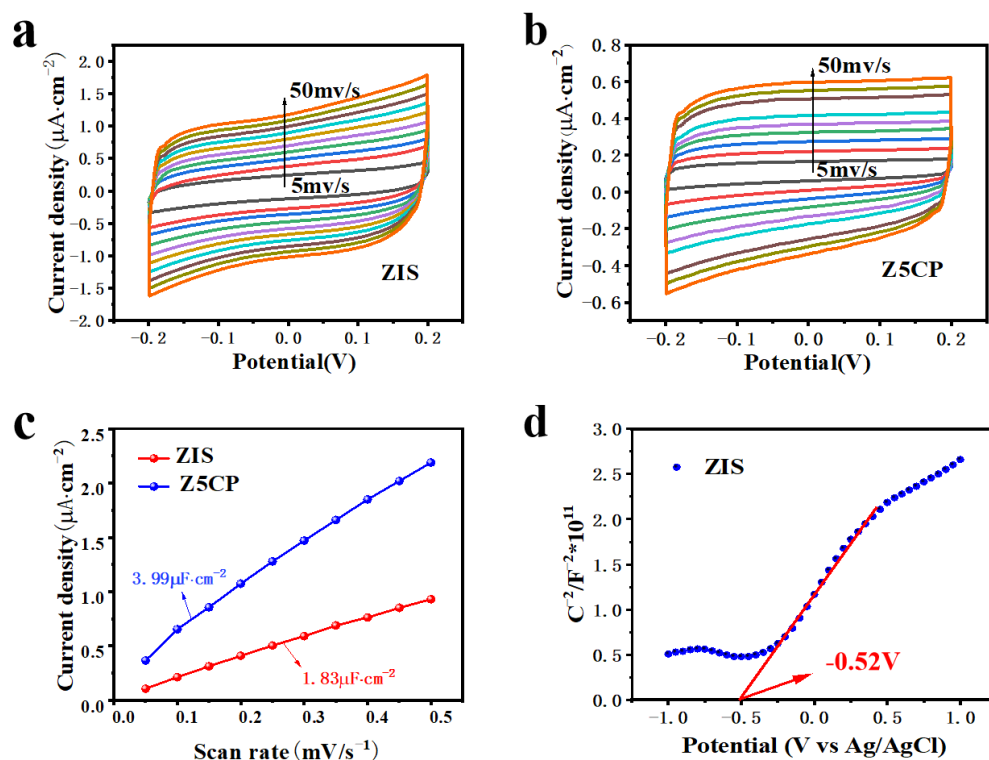
Figure 6. (**a**,**b**) Cyclic voltammetry curves of the ZIS and Z5CP. (**c**) Current density scan rate plot. (**d**) Mott−Schottky plots for ZIS.

Combined with the above experiments and characterization, we propose a viable mechanism for photocatalytic H_2 production of Z5CP under visible light. As shown in Figure 7, under visible light irradiation, Z5CP effectively absorbs the photon energy, and then the electrons on the valence band (VB) are excited and transition to the conduction band (CB), and the corresponding positive electric holes are generated on the valence band (VB). The electron (e^-) migrated to the semiconductor surface binds to the H^+ adsorbed in water to form H_2. However, ZIS has a high electrons and holes recombination rate; therefore, its photocatalytic activity is limited. Notably, Co-Pi has the excellent property of transferring photogenerated holes, and the holes of ZIS are transferred to Co-Pi and drive cycles to catalyze the $Co^{2+/3+} \rightarrow Co^{4+} \rightarrow Co^{2+/3+}$ reaction [24]. At the same time, ZIS rapidly exports holes to oxidize the sacrificial reagent of triethanolamine (TEOA); therefore, the resulting photogenerated hole (h^+) is effectively separated and consumed by it. Therefore, the photogenerated carrier separation efficiency of the composite photocatalyst Z5CP is improved, which allows more electrons to transfer to the catalyst surface to react with H^+ to produce more H_2. This is also the main factor for the significant improvement of the photocatalytic H_2 evolution performance of Z5CP composite.
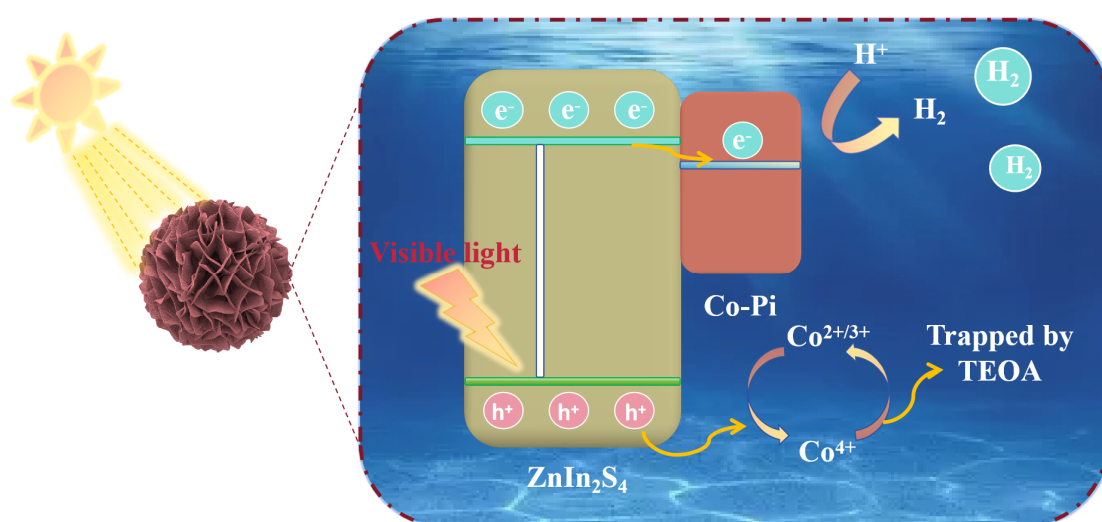
Figure 7. Mechanism diagram of Z5CP in the visible light-driven photocatalytic H_2 production reaction.

3. Experimental Section

3.1. Materials

Concentrated sulfuric acid (H_2SO_4), triethanolamine ($C_6H_{15}NO_3$, TEOA), anhydrous ethanol (C_2H_5OH), N,N-dimethylformamide (C_3H_7NO), disodium hydrogen phosphate dihydrate ($Na_2HPO_4 \cdot 2H_2O$), and sodium dihydrogen phosphate tetrahydrate ($NaH_2PO_4 \cdot 4H_2O$) are supplied by Xilong Scientific Co., Ltd. (Shantou, China). Cobalt nitrate hexahydrate ($Co(NO_3)_2 \cdot 6H_2O$), cetyltrimethylammonium bromide ($C_{19}H_{42}BrN$, CTAB), zinc nitrate hexahydrate ($Zn(NO_3)_2 \cdot 6H_2O$), indium chloride tetrahydrate ($InCl_3 \cdot 4H_2O$), and Nafion solution (5 wt%) ($C_9HF_{17}O_5S$) are supplied by Sinopharm Chemical Reagent Co., Ltd. (Shanghai, China).

3.2. Synthesis of $ZnIn_2S_4$ (ZIS)

Typically, $Zn(NO_3)_2 \cdot 6H_2O$ (304.2 mg), $InCl_3 \cdot 4H_2O$ (624.4 mg), and cetyltrimethylammonium bromide (CTAB) (230.6 mg) were added to a beaker containing 20 mL of deionized water and magnetically stirred for 30 min. Then, the thioacetamide (604.8 mg) was added to a beaker containing 10 mL deionized water and mixed to the above solution. Afterwards, the mixture was added to a Teflon liner and stirred for 30 min, and the liner was transferred to stainless steel autoclave heating in an oven at 433 K for 16 h. After cooling, the products were separated by filtration and washed several times with deionized

water and ethanol. The resulting samples were dried under vacuum at 333 K for 12 h. Ultimately, a bright yellow solid was obtained.

3.3. Synthesis of $ZnIn_2S_4$/Co-Pi (ZIS/Co-Pi)

In a typical experiment, the prepared 200 mL (0.1 mol/L) NaH_2PO_4 and 200 mL (0.1 mol/L) Na_2HPO_4 solution were mixed and adjusted with pH to around 7. Subsequently, 80 mL of neutral buffer was measured, and the calculated amount of $Co(NO_3)_2 \cdot 6H_2O$ was added to make it evenly dispersed by ultrasound. Furthermore, 40 mg of $ZnIn_2S_4$ was weighed and introduced into the aforementioned system which was then sealed using a sealing ring with several ventilation holes. Then, the system was subjected to Ar gas flow under magnetic stirring for 30 min followed by irradiation from a xenon lamp while maintaining stirring for an additional duration of 60 min after sealing. After the photodeposition, the samples were filtered with deionized water, and the samples were obtained after vacuum drying at 333 K for 12 h. The loading amount of Co-Pi in ZIS/xCo-Pi was altered by changing the amount of $Co(NO_3)_2 \cdot 6H_2O$. In the experimental design, the loading ratios of deposited Co-Pi in $ZnIn_2S_4$ are 1%, 5%, and 10%, respectively.

3.4. Activity Evaluation of Photocatalytic H_2 Evolution

Photocatalytic H_2 production was performed in a 50 mL airtight quartz reactor. In the entire quartz reactor, 5 mg of the catalyst was dispersed into a solution containing 5 mL of deionized water and 1 mL of triethanolamine (TEOA). Before the reaction, high purity Ar was injected into the quartz reactor for 30 min to exhaust the residual air in the reactor. A 300 W xenon lamp ($\lambda > 420$ nm) was selected as the light source, and after 2 h of illumination, 1 mL of gas was extracted into the gas chromatograph (thermal conductivity detector TCD, Agilent Technologies GC 7820A, Santa Clara, CA, USA) to detect the hydrogen yield obtained after the reaction. In order to evaluate the stability of ZIS/Co-Pi composite, the photocatalyst was separated and centrifuged. The recovered photocatalyst is then subjected to a subsequent cycle under the same conditions.

3.5. Characterization Methods

The morphological characteristics were tested through scanning electron microscopy (SEM, FESEM ZEISS sigma 500, Oberkochen, Batenwerburg, Germany) and transmission electron microscopy (TEM, Jeol JEM-2100F instrument, Jeol, Akishima, Tokyo). The determination of crystal structures was determined by X-ray diffraction (XRD) with Cu Kα ($\lambda = 0.15406$ nm, Bruker D8 Advance, Billerica, MA, USA). The surface composition of the samples was determined by X-ray photoelectron spectrometer (XPS, Thermo Fisher, K-Alpha, Waltham, MA, USA). The UV-visible diffuse reflectance spectrometer (DRS, Shimadzu UV-2600, Kyoto, Japan) was used to test the optical response of the catalyst. Photoluminescence (PL) spectra were obtained using a spectrofluorometer (FLS 980, Edinburgh Instruments Ltd., Edinburgh, UK) with an excitation wavelength of 500 nm. Furthermore, all the electrochemical measurements of the photocurrent, the electrochemical impedance spectra (EIS), the Mott–Schottky (MS), cyclic voltammetry (CV), and linear sweep voltammetry (LSV) curves were carried out in the three-electrode cell, in which Ag/AgCl was used as a reference electrode, a Pt wire was used as a counter electrode, and an indium in oxide (ITO) conductive glass was used with the samples as a working electrode in 0.1 M Na_2SO_4 electrolyte (pH = 7.56), all measurements were carried out on CH instruments CHI-660E electrochemical workstation (Shanghai Chenhua CHI-660E, Shanghai, China).

4. Conclusions

In summary, we synthesize spherical $ZnIn_2S_4$ nanoflower substrate material by the hydrothermal method, and reasonably construct a novel photocatalyst of indium zinc sulfide/cobalt phosphate ($ZnIn_2S_4$/Co-Pi) hybrid photocatalyst by the in situ photodeposition method. In the presence of cocatalyst cobalt phosphate (Co-Pi), the hybrid photocatalyst shows outstanding photocatalytic hydrogen evolution performance. Through changing

the photodeposition amount of Co-Pi, it is observed that the highest H_2 production rate of indium zinc sulfide ($ZnIn_2S_4$/5% Co-Pi) loaded with 5% cobalt phosphate (Co-Pi) is 3593 $\mu mol \cdot g^{-1} \cdot h^{-1}$, which is significantly higher than that of pure $ZnIn_2S_4$. The steady-state photoluminescence (PL) and electrochemical impedance spectroscopy (EIS) of the photocatalyst show that $ZnIn_2S_4$/Co-Pi composite has weaker PL intensity and lower charge transport resistance than blank $ZnIn_2S_4$, demonstrating that the hybrid photocatalyst has faster electron transfer and charge separation. Simultaneously, the larger double-layer capacitance and smaller overpotential of catalyst indicate that $ZnIn_2S_4$/Co-Pi composite has larger active area and better hydrogen evolution performance. This work makes reasonable use of the earth-abundant cocatalysts to design low-cost and efficient composite catalysts to promote the prospect of photocatalytic hydrogen evolution.

Institutional Review Board Statement: Not applicable.

Informed Consent Statement: Not applicable.

Data Availability Statement: Data are contained within the article.

Conflicts of Interest: The authors declare no conflict of interest.

References

1. Gong, Y.-N.; Zhong, W.; Li, Y.; Qiu, Y.; Zheng, L.; Jiang, J.; Jiang, H.-L. Regulating Photocatalysis by Spin-State Manipulation of Cobalt in Covalent Organic Frameworks. *J. Am. Chem. Soc.* **2020**, *142*, 16723–16731. [CrossRef]
2. Su, B.; Zheng, M.; Lin, W.; Lu, X.F.; Luan, D.; Wang, S.; Lou, X.W. S-Scheme Co_9S_8@$Cd_{0.8}Zn_{0.2}$S-DETA Hierarchical Nanocages Bearing Organic CO_2 Activators for Photocatalytic Syngas Production. *Adv. Energy Mater.* **2023**, *13*, 2203290. [CrossRef]
3. Su, Q.; Zuo, C.; Liu, M.; Tai, X. A Review on Cu_2O-Based Composites in Photocatalysis: Synthesis, Modification, and Applications. *Molecules* **2023**, *28*, 5576. [CrossRef] [PubMed]
4. Paul, R.; Zhai, Q.; Roy, A.K.; Dai, L. Charge transfer of carbon nanomaterials for efficient metal-free electrocatalysis. *Interdiscip. Mater.* **2022**, *1*, 28–50. [CrossRef]
5. Yang, F.; Hu, P.; Yang, F.; Hua, X.-J.; Chen, B.; Gao, L.; Wang, K.-S. Photocatalytic applications and modification methods of two-dimensional nanomaterials: A review. *Tungsten* **2023**. [CrossRef]
6. Camara, F.; Gavaggio, T.; Dautreppe, B.; Chauvin, J.; Pécaut, J.; Aldakov, D.; Collomb, M.-N.; Fortage, J. Electrochemical Properties of a Rhodium(III) Mono-Terpyridyl Complex and Use as a Catalyst for Light-Driven Hydrogen Evolution in Water. *Molecules* **2022**, *27*, 6614. [CrossRef] [PubMed]
7. Wan, S.; Xu, J.; Cao, S.; Yu, J. Promoting intramolecular charge transfer of graphitic carbon nitride by donor–acceptor modulation for visible-light photocatalytic H_2 evolution. *Interdiscip. Mater.* **2022**, *1*, 294–308. [CrossRef]

8.   Ma, M.-Y.; Yu, H.-Z.; Deng, L.-M.; Wang, L.-Q.; Liu, S.-Y.; Pan, H.; Ren, J.-W.; Maximov, M.Y.; Hu, F.; Peng, S.-J. Interfacial engineering of heterostructured carbon-supported molybdenum cobalt sulfides for efficient overall water splitting. *Tungsten* **2023**, *5*, 589–597. [CrossRef]

9.   Wu, K.; Shang, Y.; Li, H.; Wu, P.; Li, S.; Ye, H.; Jian, F.; Zhu, J.; Yang, D.; Li, B.; et al. Synthesis and Hydrogen Production Performance of MoP/a-TiO$_2$/Co-ZnIn$_2$S$_4$ Flower-like Composite Photocatalysts. *Molecules* **2023**, *28*, 4350. [CrossRef]

10.   Yoshimura, N.; Yoshida, M.; Kobayashi, A. Efficient Hydrogen Production by a Photoredox Cascade Catalyst Comprising Dual Photosensitizers and a Transparent Electron Mediator. *J. Am. Chem. Soc.* **2023**, *145*, 6035–6038. [CrossRef]

11.   Lu, K.-Q.; Lin, X.; Tang, Z.-R.; Xu, Y.-J. Silicon nanowires@Co$_3$O$_4$ arrays film with Z-scheme band alignment for hydrogen evolution. *Catal. Today* **2019**, *335*, 294–299. [CrossRef]

12.   Hu, N.; Cai, Y.; Li, L.; Wang, X.; Gao, J. Amino-Functionalized Titanium Based Metal-Organic Framework for Photocatalytic Hydrogen Production. *Molecules* **2022**, *27*, 4241. [CrossRef] [PubMed]

13.   Liu, Z.-Y.; Lin, Y.-D.; Hao, Y.; Chen, H.-N.; Guo, Z.-W.; Li, X.-X.; Zheng, S.-T. Recent advances in polyoxoniobate-catalyzed reactions. *Tungsten* **2022**, *4*, 81–98. [CrossRef]

14.   Liu, C.; Zhang, Q.; Zou, Z. Recent advances in designing ZnIn$_2$S$_4$-based heterostructured photocatalysts for hydrogen evolution. *J. Mater. Sci. Technol.* **2023**, *139*, 167–188. [CrossRef]

15.   Zhang, Y.; Wu, Y.; Wan, L.; Ding, H.; Li, H.; Wang, X.; Zhang, W. Hollow core–shell Co$_9$S$_8$@ZnIn$_2$S$_4$/CdS nanoreactor for efficient photothermal effect and CO$_2$ photoreduction. *Appl. Catal. B* **2022**, *311*, 121255. [CrossRef]

16.   Jiang, X.; Fan, D.; Yao, X.; Dong, Z.; Li, X.; Ma, S.; Liu, J.; Zhang, D.; Li, H.; Pu, X.; et al. Highly efficient flower-like ZnIn$_2$S$_4$/CoFe$_2$O$_4$ photocatalyst with p-n type heterojunction for enhanced hydrogen evolution under visible light irradiation. *J. Colloid Interface Sci.* **2023**, *641*, 26–35. [CrossRef]

17.   Jiang, X.; Kong, D.; Luo, B.; Wang, M.; Zhang, D.; Pu, X. Preparation of magnetically retrievable flower-like AgBr/BiOBr/NiFe$_2$O$_4$ direct Z-scheme heterojunction photocatalyst with enhanced visible-light photoactivity. *Colloids Surf. A* **2022**, *633*, 127880. [CrossRef]

18.   Shi, R.; Yang, P.; Song, X.; Wang, J.; Che, Q.; Zhang, A. ZnO flower: Self-assembly growth from nanosheets with exposed {1 1$^-$ 0 0} facet, white emission, and enhanced photocatalysis. *Appl. Surf. Sci.* **2016**, *366*, 506–513. [CrossRef]

19.   Yuan, L.; Yang, M.-Q.; Xu, Y.-J. A low-temperature and one-step method for fabricating ZnIn$_2$S$_4$–GR nanocomposites with enhanced visible light photoactivity. *J. Mater. Chem. A* **2014**, *2*, 14401. [CrossRef]

20.   Jin, P.; Wang, L.; Ma, X.; Lian, R.; Huang, J.; She, H.; Zhang, M.; Wang, Q. Construction of hierarchical ZnIn$_2$S$_4$@PCN-224 heterojunction for boosting photocatalytic performance in hydrogen production and degradation of tetracycline hydrochloride. *Appl. Catal. B* **2021**, *284*, 119762. [CrossRef]

21.   Chen, J.; Wu, S.-J.; Cui, W.-J.; Guo, Y.-H.; Wang, T.-W.; Yao, Z.-W.; Shi, Y.; Zhao, H.; Liu, J.; Hu, Z.-Y.; et al. Nickel clusters accelerating hierarchical zinc indium sulfide nanoflowers for unprecedented visible-light hydrogen production. *J. Colloid Interface Sci.* **2022**, *608*, 504–512. [CrossRef]

22.   Ding, Y.; Maitra, S.; Wang, C.; Halder, S.; Zheng, R.; Barakat, T.; Roy, S.; Chen, L.H.; Su, B.L. Vacancy defect engineering in semiconductors for solar light-driven environmental remediation and sustainable energy production. *Interdiscip. Mater.* **2022**, *1*, 213–255. [CrossRef]

23.   Busser, G.W.; Mei, B.; Pougin, A.; Strunk, J.; Gutkowski, R.; Schuhmann, W.; Willinger, M.-G.; Schlögl, R.; Muhler, M. Photodeposition of Copper and Chromia on Gallium Oxide: The Role of Co-Catalysts in Photocatalytic Water Splitting. *ChemSusChem* **2014**, *7*, 1030–1034. [CrossRef] [PubMed]

24.   Lu, K.-Q.; Qi, M.-Y.; Tang, Z.-R.; Xu, Y.-J. Earth-Abundant MoS$_2$ and Cobalt Phosphate Dual Cocatalysts on 1D CdS Nanowires for Boosting Photocatalytic Hydrogen Production. *Langmuir* **2019**, *35*, 11056–11065. [CrossRef] [PubMed]

25.   Su, H.; Wang, W. Dynamically Monitoring the Photodeposition of Single Cocatalyst Nanoparticles on Semiconductors via Fluorescence Imaging. *Anal. Chem.* **2021**, *93*, 11915–11919. [CrossRef] [PubMed]

26.   Zhao, H.; Mao, Q.; Jian, L.; Dong, Y.; Zhu, Y. Photodeposition of earth-abundant cocatalysts in photocatalytic water splitting: Methods, functions, and mechanisms. *Chin. J. Catal.* **2022**, *43*, 1774–1804. [CrossRef]

27.   Wang, M.; Liu, Y.; Li, D.; Tang, J.; Huang, W. Isoelectric point-controlled preferential photodeposition of platinum on Cu$_2$O-TiO$_2$ composite surfaces. *Chin. Chem. Lett.* **2019**, *30*, 985–988. [CrossRef]

28.   Zhang, M.; Tan, P.; Yang, L.; Zhai, H.; Liu, H.; Chen, J.; Ren, R.; Tan, X.; Pan, J. Sulfur vacancy and p-n junction synergistically boosting interfacial charge transfer and separation in ZnIn$_2$S$_4$/NiWO$_4$ heterostructure for enhanced photocatalytic hydrogen evolution. *J. Colloid Interface Sci.* **2023**, *634*, 817–826. [CrossRef]

29.   Qu, Y.; Ren, J.; Sun, D.; Yu, Y. Synergetic control of specific orientation and self-distribution of photoelectrons in micro-nano ZnIn$_2$S$_4$/black phosphorus quantum dots (BPQDs) heterojunction to enhance photocatalytic hydrogen evolution. *J. Colloid Interface Sci.* **2023**, *642*, 204–215. [CrossRef]

30.   Li, Y.; Li, S.; Meng, L.; Peng, S. Synthesis of oriented J type ZnIn$_2$S$_4$@CdIn$_2$S$_4$ heterojunction by controllable cation exchange for enhancing photocatalytic hydrogen evolution. *J. Colloid Interface Sci.* **2023**, *650*, 266–274. [CrossRef]

31.   Chong, W.-K.; Ng, B.-J.; Kong, X.Y.; Tan, L.-L.; Putri, L.K.; Chai, S.-P. Non-metal doping induced dual p-n charge properties in a single ZnIn$_2$S$_4$ crystal structure provoking charge transfer behaviors and boosting photocatalytic hydrogen generation. *Appl. Catal. B* **2023**, *325*, 122372. [CrossRef]

32. Dong, W.; Zhou, S.-A.; Ma, Y.; Chi, D.-J.; Chen, R.; Long, H.-M.; Chun, T.-J.; Liu, S.-J.; Qian, F.-P.; Zhang, K. N-doped C-coated $MoO_2/ZnIn_2S_4$ heterojunction for efficient photocatalytic hydrogen production. *Rare Met.* **2023**, *42*, 1195–1204. [CrossRef]

33. Xu, J.; Zhong, W.; Chen, F.; Wang, X.; Yu, H. In situ cascade growth-induced strong coupling effect toward efficient photocatalytic hydrogen evolution of $ReS_2/ZnIn_2S_4$. *Appl. Catal. B* **2023**, *328*, 122493. [CrossRef]

34. Wu, K.; Jiang, R.; Zhao, Y.; Mao, L.; Gu, X.; Cai, X.; Zhu, M. Hierarchical $NiCo_2S_4/ZnIn_2S_4$ heterostructured prisms: High-efficient photocatalysts for hydrogen production under visible-light. *J. Colloid Interface Sci.* **2022**, *619*, 339–347. [CrossRef] [PubMed]

35. Feng, X.; Shang, H.; Zhou, J.; Ma, X.; Gao, X.; Wang, D.; Zhang, B.; Zhao, Y. Heterostructured core–shell $CoS_{1.097}@ZnIn_2S_4$ nanosheets for enhanced photocatalytic hydrogen evolution under visible light. *Chem. Eng. J.* **2023**, *457*, 141192. [CrossRef]

36. Li, Q.; Lu, Q.; Guo, E.; Wei, M.; Pang, Y. Hierarchical $Co_9S_8/ZnIn_2S_4$ Nanoflower Enables Enhanced Hydrogen Evolution Photocatalysis. *Energy Fuels* **2022**, *36*, 4541–4548. [CrossRef]

37. Zhao, F.; Zhang, M.; Yan, D.; Hu, X.; Fan, J.; Sun, T.; Liu, E. S-Scheme Co_9S_8 Nanoflower/Red Phosphorus Nanosheet Heterojunctions for Enhanced Photocatalytic H_2 Evolution. *ACS Appl. Nano Mater.* **2023**, *6*, 14478–14487. [CrossRef]

38. Liang, Q.; Gao, W.; Liu, C.; Xu, S.; Li, Z. A novel 2D/1D core-shell heterostructures coupling MOF-derived iron oxides with $ZnIn_2S_4$ for enhanced photocatalytic activity. *J. Hazard. Mater.* **2020**, *392*, 122500. [CrossRef]

39. Jiang, X.; Wang, Z.; Zhang, M.; Wang, M.; Wu, R.; Shi, X.; Luo, B.; Zhang, D.; Pu, X.; Li, H. A novel direct Z-scheme heterojunction $BiFeO_3/ZnFe_2O_4$ photocatalyst for enhanced photocatalyst degradation activity under visible light irradiation. *J. Alloys Compd.* **2022**, *912*, 165185. [CrossRef]

40. Ge, L.; Han, C.; Xiao, X.; Guo, L. In situ synthesis of cobalt–phosphate (Co–Pi) modified g-C_3N_4 photocatalysts with enhanced photocatalytic activities. *Appl. Catal. B* **2013**, *142–143*, 414–422. [CrossRef]

41. Xu, J.; Li, Q.; Sui, D.; Jiang, W.; Liu, F.; Gu, X.; Zhao, Y.; Ying, P.; Mao, L.; Cai, X.; et al. In Situ Photodeposition of Cobalt Phosphate (CoH_xPO_y) on $CdIn_2S_4$ Photocatalyst for Accelerated Hole Extraction and Improved Hydrogen Evolution. *Nanomaterials* **2023**, *13*, 420. [CrossRef] [PubMed]

42. Zhang, G.; Chen, D.; Li, N.; Xu, Q.; Li, H.; He, J.; Lu, J. Construction of Hierarchical Hollow $Co_9S_8/ZnIn_2S_4$ Tubular Heterostructures for Highly Efficient Solar Energy Conversion and Environmental Remediation. *Angew. Chem. Int. Ed.* **2020**, *59*, 8255–8261. [CrossRef] [PubMed]

43. Lakhera, S.K.; Vijayarajan, V.S.; Rishi Krishna, B.S.; Veluswamy, P.; Neppolian, B. Cobalt phosphate hydroxide loaded g-C_3N_4 photocatalysts and its hydrogen production activity. *Int. J. Hydrogen Energy* **2020**, *45*, 7562–7573. [CrossRef]

44. Liu, Z.-G.; Wei, Y.; Xie, L.; Chen, H.-Q.; Wang, J.; Yang, K.; Zou, L.-X.; Deng, T.; Lu, K.-Q. Decorating CdS with cobaltous hydroxide and graphene dual cocatalyst for photocatalytic hydrogen production coupled selective benzyl alcohol oxidation. *Mol. Catal.* **2024**, *553*, 113738. [CrossRef]

45. Wei, Y.; Hao, J.-G.; Zhang, J.-L.; Huang, W.-Y.; Ouyang, S.-B.; Yang, K.; Lu, K.-Q. Integrating $Co(OH)_2$ nanosheet arrays on graphene for efficient noble-metal-free EY-sensitized photocatalytic H_2 evolution. *Dalton Trans.* **2023**, *52*, 13923–13929. [CrossRef]

46. Ai, G.; Mo, R.; Li, H.; Zhong, J. Cobalt phosphate modified TiO_2 nanowire arrays as co-catalysts for solar water splitting. *Nanoscale* **2015**, *7*, 6722–6728. [CrossRef]

47. Jiang, Q.; Sun, L.; Bi, J.; Liang, S.; Li, L.; Yu, Y.; Wu, L. MoS_2 Quantum Dots-Modified Covalent Triazine-Based Frameworks for Enhanced Photocatalytic Hydrogen Evolution. *ChemSusChem* **2018**, *11*, 1108–1113. [CrossRef]

48. Li, X.-X.; Liu, X.-C.; Liu, C.; Zeng, J.-M.; Qi, X.-P. Co_3O_4/stainless steel catalyst with synergistic effect of oxygen vacancies and phosphorus doping for overall water splitting. *Tungsten* **2022**, *5*, 100–108. [CrossRef]

49. Mu, P.; Zhou, M.; Yang, K.; Chen, X.; Yu, Z.; Lu, K.; Huang, W.; Yu, C.; Dai, W. $Cd_{0.5}Zn_{0.5}S/CoWO_4$ Nanohybrids with a Twinning Homojunction and an Interfacial S-Scheme Heterojunction for Efficient Visible-Light-Induced Photocatalytic CO_2 Reduction. *Inorg. Chem.* **2021**, *60*, 14854–14865. [CrossRef]

50. Jiang, X.; Gong, H.; Liu, Q.; Song, M.; Huang, C. In situ construction of $NiSe/Mn_{0.5}Cd_{0.5}S$ composites for enhanced photocatalytic hydrogen production under visible light. *Appl. Catal. B* **2020**, *268*, 118439. [CrossRef]

51. Li, M.; Zhang, D.; Zhou, h.; Sun, K.; Ma, X.; Dong, M. Construction of hollow tubular $Co_9S_8/ZnSe$ S-scheme heterojunctions for enhanced photocatalytic H_2 evolution. *Int. J. Hydrogen Energy* **2023**, *48*, 5126–5137. [CrossRef]

52. Li, J.-Y.; Qi, M.-Y.; Xu, Y.-J. Efficient splitting of alcohols into hydrogen and C–C coupled products over ultrathin Ni-doped $ZnIn_2S_4$ nanosheet photocatalyst. *Chin. J. Catal.* **2022**, *43*, 1084–1091. [CrossRef]

53. Chong, W.-K.; Ng, B.-J.; Lee, Y.J.; Tan, L.-L.; Putri, L.K.; Low, J.; Mohamed, A.R.; Chai, S.-P. Self-activated superhydrophilic green $ZnIn_2S_4$ realizing solar-driven overall water splitting: Close-to-unity stability for a full daytime. *Nat. Commun.* **2023**, *14*, 7676. [CrossRef]

54. Jiang, J.; Xiong, Z.; Wang, H.; Liao, G.; Bai, S.; Zou, J.; Wu, P.; Zhang, P.; Li, X. Sulfur-doped g-C_3N_4/g-C_3N_4 isotype step-scheme heterojunction for photocatalytic H_2 evolution. *J. Mater. Sci. Technol.* **2022**, *118*, 15–24. [CrossRef]

55. Yan, W.; Zhang, Y.; Bi, Y. Subnanometric Bismuth Clusters Confined in Pyrochlore-$Bi_2Sn_2O_7$ Enable Remarkable CO_2 Photoreduction. *Angew. Chem. Int. Ed.* **2023**, *63*, e202316459. [CrossRef] [PubMed]

56. Wang, X.-K.; Liu, J.; Zhang, L.; Dong, L.-Z.; Li, S.-L.; Kan, Y.-H.; Li, D.-S.; Lan, Y.-Q. Monometallic Catalytic Models Hosted in Stable Metal–Organic Frameworks for Tunable CO_2 Photoreduction. *ACS Catal.* **2019**, *9*, 1726–1732. [CrossRef]

57. Lu, K.-Q.; Li, Y.-H.; Zhang, F.; Qi, M.-Y.; Chen, X.; Tang, Z.-R.; Yamada, Y.M.A.; Anpo, M.; Conte, M.; Xu, Y.-J. Rationally designed transition metal hydroxide nanosheet arrays on graphene for artificial CO_2 reduction. *Nat. Commun.* **2020**, *11*, 5181. [CrossRef]

58. Guan, X.; Qian, Y.; Zhang, X.; Jiang, H.L. Enaminone-Linked Covalent Organic Frameworks for Boosting Photocatalytic Hydrogen Production. *Angew. Chem. Int. Ed.* **2023**, *62*, e202306135. [CrossRef]

59. Gao, J.-X.; Tian, W.-J.; Zhang, H.-Y. Progress of Nb-containing catalysts for carbon dioxide reduction: A minireview. *Tungsten* **2022**, *4*, 284–295. [CrossRef]

60. Zou, J.; Wu, S.; Liu, Y.; Sun, Y.; Cao, Y.; Hsu, J.-P.; Shen Wee, A.T.; Jiang, J. An ultra-sensitive electrochemical sensor based on 2D g-C_3N_4/CuO nanocomposites for dopamine detection. *Carbon* **2018**, *130*, 652–663. [CrossRef]

61. Hu, M.; Wu, C.; Feng, S.; Hua, J. A High Crystalline Perylene-Based Hydrogen-Bonded Organic Framework for Enhanced Photocatalytic H_2O_2 Evolution. *Molecules* **2023**, *28*, 6850. [CrossRef] [PubMed]

62. Lu, K.-Q.; Chen, Y.; Xin, X.; Xu, Y.-J. Rational utilization of highly conductive, commercial Elicarb graphene to advance the graphene-semiconductor composite photocatalysis. *Appl. Catal. B* **2018**, *224*, 424–432. [CrossRef]

63. Su, B.; Kong, Y.; Wang, S.; Zuo, S.; Lin, W.; Fang, Y.; Hou, Y.; Zhang, G.; Zhang, H.; Wang, X. Hydroxyl-Bonded Ru on Metallic TiN Surface Catalyzing CO_2 Reduction with H_2O by Infrared Light. *J. Am. Chem. Soc.* **2023**, *145*, 27415–27423. [CrossRef]

64. Luo, D.; Peng, L.; Wang, Y.; Lu, X.; Yang, C.; Xu, X.; Huang, Y.; Ni, Y. Highly efficient photocatalytic water splitting utilizing a WO_3-x/$ZnIn_2S_4$ ultrathin nanosheet Z-scheme catalyst. *J. Mater. Chem. A* **2021**, *9*, 908–914. [CrossRef]

65. Tang, C.; Bao, T.; Li, S.; Wang, X.; Rao, H.; She, P.; Qin, J.-S. Bioinspired 3D penetrating structured micro-mesoporous NiCoFe-LDH@$ZnIn_2S_4$ Z-scheme heterojunction for simultaneously photocatalytic H_2 evolution coupled with benzylamine oxidation. *Appl. Catal. B* **2024**, *342*, 123384. [CrossRef]

66. Li, J.; Li, M.; Jin, Z. Rational design of a cobalt sulfide/bismuth sulfide S-scheme heterojunction for efficient photocatalytic hydrogen evolution. *J. Colloid Interface Sci.* **2021**, *592*, 237–248. [CrossRef]

67. Li, M.; Li, J.; Jin, Z. Synergistic effect of MoS_2 over WP photocatalyst for promoting hydrogen production. *J. Solid State Chem.* **2020**, *288*, 121419. [CrossRef]

68. Wu, Z.; Yuan, X.; Zeng, G.; Jiang, L.; Zhong, H.; Xie, Y.; Wang, H.; Chen, X.; Wang, H. Highly efficient photocatalytic activity and mechanism of Yb^{3+}/Tm^{3+} codoped In_2S_3 from ultraviolet to near infrared light towards chromium (VI) reduction and rhodamine B oxidative degradation. *Appl. Catal. B* **2018**, *225*, 8–21. [CrossRef]